Journal of Fluids and Structures 24 (2008) 151–163

JOURNAL OF
FLUIDS AND
STRUCTURES

www.elsevier.com/locate/jfs

Brief communication

An assessment of some effects of the nonsmoothness of the Leishman–Beddoes dynamic stall model on the nonlinear dynamics of a typical aerofoil section

U. Galvanetto*, J. Peiró, C. Chantharasenawong

Department of Aeronautics, Imperial College London, South Kensington Campus, London SW7 2AZ, UK

Received 25 September 2006; accepted 16 July 2007

Abstract

We investigate the dynamic behaviour of the typical airfoil section modelled structurally by linear springs in pitch and plunge with the aerodynamic loading represented by our interpretation of the state-space version of the Leishman–Beddoes semi-empirical model. Similarly to other semi-empirical models of dynamic stall, this model represents the nonlinear component of the unsteady aerodynamic loading on the airfoil by a series of equations, with empirical coefficients, devised specifically for each of the relevant dynamic stall flow states. Given this piecewise definition of the loading, we pay particular attention to the description of the discontinuities of the model and to their effect on the dynamics of the system through phase plots, Poincaré sections and bifurcation diagrams. These results show that the model is sensitive to small variations of some of the parameters of the model. They also show that prohibitively small timesteps are required to obtain numerically converged Poincaré maps. We advocate the use of event detection techniques for the numerical integration of the equations of motion to reduce this severe timestep restriction.

Keywords: Aeroelasticity; Dynamic stall; Nonlinear dynamics; Nonsmooth dynamical systems; Event detection; Computational methods

1. Introduction

The term dynamic stall usually refers to an unsteady flow characterized by the formation, convection and shedding of a vortex on the suction side of an aerofoil. Dynamic stall may affect the aerodynamic performance of helicopter blades, turbomachinery compressor blades, wind turbines and other streamlined structures operating at high angles of incidence. It could also reduce fatigue life of many modern lightweight blades through the induced vibrations. This phenomenon has been described in excellent reviews (McCroskey, 1982; Ericsson and Reding, 1988; Leishman, 2006).

The main events in the flow development around the aerofoil during a dynamic stall cycle are: (i) the dynamic lift exceeds maximum static lift at the static stall angle, (ii) a vortex is formed at the leading edge and its formation marks the beginning of the moment stall, (iii) the vortex grows in strength, is convected along the surface, reaches the trailing edge and begins its detachment when the lift stalls, (iv) finally, flow reattachment begins when the angle of incidence is

---

*Corresponding author. Tel.: +44 2075945150; fax: +44 2075848120.
E-mail address: u.galvanetto@imperial.ac.uk (U. Galvanetto).

0889-9746/$ - see front matter
doi:10.1016/j.jfluidstructs.2007.07.008

low enough again. The unsteady aerodynamic loading is significantly different from the static one for the same angles of incidence. The presence of an attached vortex on the suction side of the aerofoil generates a higher lift whereas the detachment or shedding of this vortex results in a substantial lift reduction.

Dynamic stall in lifting surfaces involves complex separated, even transitional, three-dimensional flows. Numerical simulations of these flows are possible but they are very expensive and are not always able to predict the physics accurately. Therefore simplified blade element methods in combination with two-dimensional empirical stall models are routinely used for engineering design purposes both in helicopter rotors (Leishman, 2006) and wind turbines (Burton et al., 2001). Tan and Carr (1996) present a comparison of simulations obtained with these methods with three-dimensional data.

Several semi-empirical dynamical stall models have been proposed. Amongst these we could mention those devised by ONERA (Petot, 1989), Boeing (Gormont, 1973), Johnson (1970), and Gangwani (1982). We have chosen the state-space formulation of the Leishmann–Beddoes (LB) model (Leishman and Beddoes, 1986, 1989) since it exhibits the nonsmoothness that we are seeking to investigate and also because this model or its modifications (Hansen et al., 2004; Larsen et al., 2007) are widely used in engineering applications.

The purpose of this paper is to couple the LB model with a linear structural model of an aerofoil free to move in pitch and plunge to investigate and understand the dynamics of the system for varying parameter values using tools from the theory of dynamical systems. A similar approach has been adopted by other authors to investigate other dynamic stall models [e.g. Lee et al. (1998), Price and Keleris (1996), Li and Fleeter (2003)]. However, our main interest and the novel aspect of this work is the analysis of the aeroelastic system as a nonsmooth system.

The dynamics of nonsmooth dynamical systems is a fast growing research field, see for instance the book by di Bernardo et al. (2007) for an overview. The complexity of the LB model and its relatively large size prevent us from using some of the powerful theories currently under development for the analysis of such systems. Nonetheless, some of the effects of the nonsmoothness present in the LB model on the dynamics of the aerofoil will be investigated.

We have deliberately chosen the structural model to be linear so as to ensure that the nonlinear behaviour is exclusively due to the aerodynamics loading represented by the LB model. An extensive discussion of structural nonlinearities can be found in the review article by Lee et al. (1998).

The main objectives of the paper are to investigate the dynamics induced by the LB model on a two degree of freedom aerofoil section and to show some of the effects of the discontinuities on such dynamics. More importantly, the authors aim to highlight that a suitable handling of the discontinuities, often referred to as either event detection or event location (Shampine et al., 1991), is required for a numerical integration of nonsmooth systems to produce an accurate representation of their dynamic behaviour.

The paper is organized as follows. Section 2 presents the governing equations of motion. Section 3 describes our interpretation of the LB model and its implementation. Section 4 discusses the treatment of the effective angle of incidence and its derivative in the presence of pitch motion and its implications to the solution of the coupled fluid–structure system. Finally, Section 5 presents the analysis of the aeroelastic system from the perspective of the theory of dynamical systems, discusses its behaviour and sensitivity to some parameters of the model, and addresses the effect of discontinuities in the performance of the numerical solver `ode45` (Shampine and Reichelt, 1997) used to integrate the equations of motion.

2. Equations of motion of the aerofoil

The mechanical model used here is the typical two-dimensional aerofoil section in a horizontal flow of undisturbed speed U, as shown in Fig. 1. The aerofoil can move in the vertical direction (plunge) and rotate in the plane of the figure (pitch). The plunge deflection of the elastic axis is denoted by h, taken to be positive in the downward direction, and α is the pitch angle about the elastic axis, taken to be positive nose-up (clockwise according to the orientation of Fig. 1). The chord length is denoted by c and $b = c/2$ represents the mid-chord length. The elastic axis is located at a distance $a_h b$ from the mid-chord, while the mass centre is located at a distance $x_\alpha b$ along the chord from the elastic axis. Both distances are positive when measured towards the trailing edge of the aerofoil. The structural behaviour is modelled by means of linear bending and torsional springs and dampers which are attached to the elastic axis.

The equations of motion have been derived in many textbooks of aeroelasticity [see Fung (1993)] and can be written in nondimensional form as

$$\xi'' + x_\alpha \alpha'' + 2\zeta_\xi \frac{\bar{\omega}}{U^*}\xi' + \left(\frac{\bar{\omega}}{U^*}\right)^2 \xi = -\frac{1}{\pi\mu} C_L(S), \tag{1}$$

$$\frac{x_\alpha}{r_\alpha^2}\xi'' + \alpha'' + 2\frac{\zeta_\alpha}{U^*}\alpha' + \frac{1}{U^{*^2}}\alpha = \frac{(0.5 + a_h)}{\mu\pi r_\alpha^2}[C_L(S)\cos\alpha + C_D(S)\sin\alpha] + \frac{2}{\pi\mu r_\alpha^2} C_M(S), \tag{2}$$

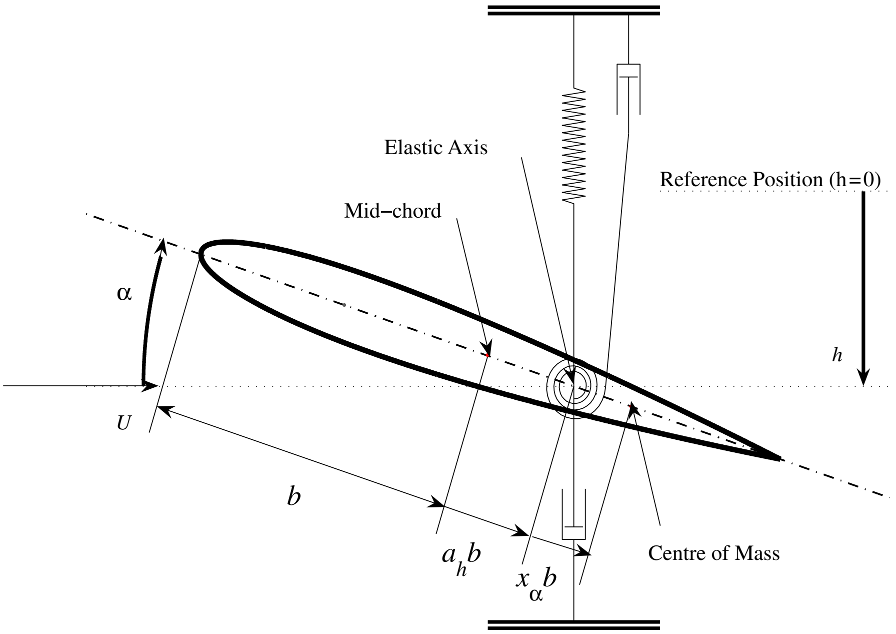

Fig. 1. A sketch of the typical aerofoil section at an angle of incidence α and a deflection $h \neq 0$.

where the angle of incidence, α, is measured in radians and the plunge displacement is represented by the nondimensional quantity, $\xi = 2h/c$. The prime denotes differentiation with respect to the nondimensional time $S = 2Vt/c$. The symbols C_L, C_D and C_M denote the coefficients of lift, drag and pitching moment about the aerofoil quarter chord, respectively, and are assumed to be a function of the degrees of freedom and their first and second time derivatives. The other parameters are: the ratio of natural frequencies in plunge and pitch $\bar{\omega}$, the nondimensional damping coefficients in plunge ζ_ξ and in pitch ζ_α, the nondimensional airspeed U^*, the aerofoil to air mass ratio μ, and the aerofoil radius of gyration r_α.

3. LB dynamic stall model

This section describes our interpretation of the state-space form of the LB model as described by Leishman and Nguyen (1988), Leishman and Crouse (1989) and Crouse and Leishman (1992). The main advantage of using the state-space form is that it can be appended to the structural model to construct a system of ordinary differential equations representing the dynamical system. This model was originally developed for the aerodynamic analysis of rotor blades by Beddoes (1983) and later revised by Leishman and Beddoes (1986, 1989).

The inputs to the system consist of the effective pitch angle, $\hat{\alpha}$, and the nondimensional pitch rate, q. Since these are the only inputs to the dynamic stall model, they must also include the effects of plunging motions for an aerofoil with two degrees of freedom. Appropriate definitions of $\hat{\alpha}$ and q are given and further discussed in Section 4. Finally, the dynamic stall model is represented by a set of ODEs of the form

$$\mathbf{x}' = \mathbf{f}(\mathbf{x}, \hat{\alpha}, q), \tag{3}$$

and the resulting aerodynamic coefficients are given by

$$C_i = g_i(\mathbf{x}, \hat{\alpha}, q), \quad i = N, M, C, \tag{4}$$

where $\mathbf{x}' = \mathrm{d}\mathbf{x}/\mathrm{d}S$. The state vector is $\mathbf{x} = [x_1, x_2, \ldots, x_n]^{\mathrm{T}}$, and n is the number of aerodynamic states. The lift and drag are aerodynamic forces which are perpendicular and parallel to the direction of flow, respectively. However, the LB model uses a different frame of reference and instead computes the normal force C_N and chord force C_C, which act perpendicular and along the aerofoil chordline, respectively. Eventually, forces can be resolved into either frame of reference for a given angle of incidence α

$$C_L = C_N \cos\alpha - C_C \sin\alpha, \quad C_D = C_N \sin\alpha + C_C \cos\alpha. \tag{5,6}$$

The LB model consists of three parts, the unsteady attached flow, the trailing edge separation, and vortex induced airloads. The total airloads are given by

$$C_N = C_N^I + C_N^f + C_N^v, \quad C_M = C_M^I + C_M^f + C_M^v, \quad C_C = C_C^f, \tag{7,8,9}$$

where the superscripts I, f and v refer in turn to the attached flow impulsive terms, the trailing edge separation and the vortex induced loads.

3.1. Static airloads (Kirchhoff theory)

The Kirchhoff theory is used in the LB model to calculate the aerodynamic forces under steady conditions. It uses the trailing edge separation point to determine the loss in normal force with respect to the ideal flow scenario. It gives the position of the trailing edge separation point, f, as a function of $\hat{\alpha}$ and α_1 as

$$f(\hat{\alpha}, \alpha_1) = \begin{cases} 1.00 - 0.30\exp\left(\dfrac{|\hat{\alpha}| - \alpha_1}{S_1}\right) & \text{if } |\hat{\alpha}| \leqslant \alpha_1, \\ 0.04 + 0.66\exp\left(\dfrac{\alpha_1 - |\hat{\alpha}|}{S_2}\right) & \text{if } |\hat{\alpha}| \geqslant \alpha_1, \end{cases} \tag{10}$$

where α_1 is defined as the point where $f(\alpha_1, \alpha_1) = 0.70$ and it is meant to closely correspond to the aerofoil static stall angle of incidence. The condition $f = 1$ represents fully attached flow, while $f = 0$ represents fully separated flow.

The static normal force, pitching moment, and chord force are given by

$$C_{N_{\text{static}}} = C_{N\alpha}\hat{\alpha}\left(\frac{1 + \sqrt{f(\hat{\alpha}, \alpha_1)}}{2}\right)^2, \tag{11}$$

$$C_{M_{\text{static}}} = \{K_0 + K_1[1 - f(\hat{\alpha}, \alpha_1)] + K_2 \sin(\pi[f(\hat{\alpha}, \alpha_1)]^{m^*})\} C_{N_{\text{static}}}, \tag{12}$$

$$C_{C_{\text{static}}} = \eta C_{N\alpha}\hat{\alpha}^2 \sqrt{f(\hat{\alpha}, \alpha_1)}. \tag{13}$$

The parameters $C_{N\alpha}$, K_0, K_1, K_2, S_1 and S_2 are functions of the free-stream Mach number and are determined from static test data. These data are available for the NACA0012 aerofoil section (Leishman and Beddoes, 1986). The slightly modified set of parameters used here is given in Table 1 of Appendix B. From the same reference, we get $m^* = 2$ and $\eta = 0.97$.

3.2. Attached flow components

The normal forces and pitching moments under attached flow are written as

$$C_N^I = \frac{4}{M}\left(\frac{c}{2V}\right)(a_{33}x_3 + \dot{\alpha}) + \frac{1}{M}\left(\frac{c}{2V}\right)(a_{44}x_4 + q), \tag{14}$$

$$C_N^C = C_{N\alpha}\left(\frac{2V}{c}\right)\beta^2(A_1 b_1 x_1 + A_2 b_2 x_2), \tag{15}$$

$$C_M^I = \frac{-1}{M}(A_3 a_{55} x_5 + A_4 a_{66} x_6 + \dot{\alpha}) - \frac{7}{12M}\left(-\frac{1}{K_{qM} T_I} x_8 + q\right), \tag{16}$$

$$C_M^C = \left[\frac{1}{4} - x_\alpha(M)\right] C_N^C - \frac{\pi}{8} b_5 \beta \frac{2V}{c} x_7, \tag{17}$$

with superscript I indicating the impulsive terms and superscript C for the circulatory terms. The states $x_1, x_2, \ldots, x_8$ are the solutions of the system of linear ODEs

$$(\mathbf{x}^*)' = \mathbf{A}\mathbf{x}^* + \mathbf{B}\begin{Bmatrix} \hat{\alpha} \\ q \end{Bmatrix}, \tag{18}$$

where $\mathbf{x}^* = [x_1, x_2, \ldots, x_8]^{\mathrm{T}}$. The constant matrices $\mathbf{A}$, and $\mathbf{B}$ are given in Appendix A.

3.3. Trailing edge separation components

The trailing edge separation is modelled in a similar way to the Kirchhoff theory in Section 3.1. By introducing three new state variables x_9, x_{10} and x_{12} which are the solutions of the system of ODEs representing the delayed normal force, the dynamic trailing edge separation point, and the substitute dynamic trailing edge separation point, respectively, the aerodynamic forces are given by

$$C_N^f = C_N^C\left(\frac{1+\sqrt{x_{10}}}{2}\right)^2, \tag{19}$$

$$C_M^f = [K_0 + K_1(1-\hat{x}) + K_2\sin(\pi\hat{x}^m)]C_N^C\left(\frac{1+\sqrt{\hat{x}}}{2}\right)^2, \tag{20}$$

$$C_C^f = \eta C_{N\alpha}\left(\frac{C_N^C}{C_{N\alpha}}\right)^2\sqrt{x_{10}}, \tag{21}$$

where in Eq. (20), the variable $\hat{x}$ is

$$\hat{x} = \begin{cases} x_{10} & \text{if } x_{10} > x_{12}, \\ x_{12} & \text{if } x_{10} \leqslant x_{12}. \end{cases} \tag{22}$$

Eqs. (19)–(21) are very similar to those in Section 3.1, but here the variable x_{10} introduces a dynamic effect which is not present in the static case.

The states x_9, x_{10} and x_{12} are solutions of the system of ODEs

$$x_9' = \frac{(C_N^C + C_N^I) - x_9}{T_P}, \quad x_{10}' = \frac{f\left(\dfrac{x_9}{C_{N\alpha}}, \alpha_1\right) - x_{10}}{T_f}, \quad x_{12}' = \frac{f(\hat{\alpha}, \alpha_1) - x_{12}}{0.63T_{f0}}, \tag{23,24,25}$$

where the trailing edge separation point function, $f(\hat{\alpha}, \alpha_1)$, has been defined in Eq. (10).

We should remark that the numbering of these states is consistent with the original numbering used by Leishman and Crouse (1989). The "missing" variable x_{11} will be introduced later in Section 3.4. The variations of parameters T_f and α_1 are explained in the following section. The original values of the parameters T_{f0} and α_{10} are given in Table 1.

3.3.1. Vortex shedding phase ($|x_9| \geqslant C_{N1}$)

This phase occurs when the leading edge pressure reaches the critical value C_{N1} defined as the critical normal force. If $|x_9| = C_{N1}$ and $|x_9|$ is increasing, then a vortex is shed from the leading edge and the vortex time, τ_v, starts ($\tau_v = 0$). The vortex time τ_v progresses at the same rate as the nondimensional time S. The parameter T_{vl} is defined as the time required for the vortex to travel one chord length. The variation of parameter T_f during the vortex shedding phase is given by

$$T_f = \begin{cases} 3T_{f0} & \text{if } 0 \leqslant \tau_v \leqslant T_{vl} \text{ and } \alpha\alpha' \geqslant 0, \\ \frac{1}{3}T_{f0} & \text{if } T_{vl} < \tau_v \leqslant 2T_{vl} \text{ and } \alpha\alpha' \geqslant 0, \\ \frac{1}{2}T_{f0} & \text{if } 0 \leqslant \tau_v \leqslant 2T_{vl} \text{ and } \alpha\alpha' < 0, \\ 4T_{f0} & \text{if } 2T_{vl} < \tau_v. \end{cases} \tag{26}$$

The parameter α_1 does not depend on τ_v and it is given by

$$\alpha_1 = \begin{cases} \alpha_{10} & \text{if } \alpha\alpha' \geqslant 0, \\ \alpha_{10} - (1-x_{10})^{0.25}\delta_{\alpha_1} & \text{if } \alpha\alpha' < 0, \end{cases} \tag{27}$$

where δ_{α_1} is a function of M given in Table 1.

3.3.2. Flow reattachment phase ($|x_9| < C_{N1}$)

This phase is said to have begun when $|x_9| = C_{N1}$ and $|x_9|$ is decreasing. This is taken into account by choosing

$$T_f = \begin{cases} T_{f0} & \text{if } x_{10} \geqslant 0.7, \\ 2T_{f0} & \text{if } x_{10} < 0.7, \end{cases} \tag{28}$$

$$\alpha_1 = \alpha_{10}. \tag{29}$$

3.4. Vortex induced airloads

The final part of the model corresponds to the vortex induced airloads. The normal force and pitching moment generated by the vortex are given by

$$C_N^v = x_{11}, \tag{30}$$

$$C_M^v = \begin{cases} -0.25\left[1 - \cos\left(\dfrac{\pi \tau_v}{T_{vl}}\right)\right] x_{11} & \text{if } \tau_v \leqslant 2T_{vl}, \\ 0 & \text{if } \tau_v > 2T_{vl}, \end{cases} \tag{31}$$

where state x_{11} is the solution of the final ODE of the system

$$x'_{11} = \begin{cases} c'_v - \dfrac{x_{11}}{T_v} & \text{if } \alpha c'_v \geqslant 0 \text{ and } 0 < \tau_v < 2T_{vl}, \\ -\dfrac{x_{11}}{T_v} & \text{otherwise.} \end{cases} \tag{32}$$

The vortex feed, c_v, determines the strength of vortex induced normal force and is defined as the instantaneous excess normal force, $c_v = C_N^C - C_N^f$. Negative vortex feed is not allowed, therefore Eq. (32) has two forms, depending on the direction of the vortex feed as determined by the sign of the term $\alpha c'_v$ (Björck, 2000). Its derivative, c'_v, can therefore be derived from Eqs. (15) and (19) as

$$c'_v = -C_{N\alpha}\left(\frac{2V}{c}\right)\beta^2(A_1 b_1 x_1 + A_2 b_2 x_2)\frac{x'_{10}}{4}\left(1 + \frac{1}{\sqrt{x_{10}}}\right) + C_{N\alpha}\frac{2V}{c}\beta^2[A_1 b_1 x'_1 + A_2 b_2 x'_2]\left[1 - \left(\frac{1+\sqrt{x_{10}}}{2}\right)^2\right]. \tag{33}$$

The rate of change of x_{11} in Eq. (32) is controlled by the parameter T_v. This parameter is also assumed to change according to the flow condition and its variation during the vortex shedding phase ($|x_9| \geqslant C_{N1}$) is given by

$$T_v = \begin{cases} T_{v0} & \text{if } 0 \leqslant \tau_v \leqslant T_{vl} \text{ and } \alpha\alpha' \geqslant 0, \\ 0.25T_{v0} & \text{if } T_{vl} < \tau_v \leqslant 2T_{vl} \text{ and } \alpha\alpha' \geqslant 0, \\ 0.50T_{v0} & \text{if } 0 \leqslant \tau_v \leqslant 2T_{vl} \text{ and } \alpha\alpha' < 0, \\ 0.90T_{v0} & \text{if } 2T_{vl} < \tau_v. \end{cases} \tag{34}$$

Finally, the flow reattachment phase ($|x_9| < C_{N1}$) is characterized by $T_v = T_{v0}$.

A more detailed description of our interpretation of the LB model with its full validation is given by Chantharasenawong (2007).

4. Remarks about the coupling of the structural and fluid models

A critical issue, often neglected in the existing literature, is the definition of the time derivative of the effective angle of incidence. The effective angle of incidence, $\hat{\alpha}$, is the angle which has to be provided as input to the LB model and usually contains information concerning the geometric angle of incidence, α, and the angular and vertical velocities, α', ξ'. Using the quasi-steady approach (Parameswaran and Baeder, 1995), the effective angle of incidence has the form

$$\hat{\alpha} = \hat{\alpha}(\alpha, \alpha', \xi'). \tag{35}$$

The LB model also requires the pitch rate, q, that should be calculated as the derivative of the above expression, and therefore assumes the form

$$q = q(\alpha, \alpha', \alpha'', \xi', \xi''). \tag{36}$$

The coefficients C_L and C_M depend on the effective angle of incidence and its time derivative and the presence of the term $C_L(\hat{\alpha}, q)$ makes the system of ODEs implicit and therefore more difficult and expensive to solve.

In the present work the effective angle of incidence is defined as

$$\hat{\alpha} = \tan^{-1}\left[\frac{\sin\alpha + \xi'\cos\alpha + \alpha'(a_h + 0.5)}{\cos\alpha - \xi'\sin\alpha}\right]. \tag{37}$$

However, we will neglect the acceleration terms α'' and ξ'' in the expression for the pitch rate that is given by

$$q = 2\alpha'\frac{1 + (\xi')^2 + \alpha'(0.5 + a_h)(\sin\alpha + \xi'\cos\alpha)}{1 + (\xi')^2 + 2\alpha'(0.5 + a_h)(\sin\alpha + \xi'\cos\alpha) + [\alpha'(0.5 + a_h)]^2}, \tag{38}$$

where a_h is shown in Fig. 1. This is advantageous because it renders the system explicit and permits the use of standard numerical solvers. The introduction of this simplification appears to be common practice [e.g. Mahajan et al. (1993), Lee et al. (1998)] but it might have an impact on the dynamic behaviour of the system which deserves further investigation.

The nondimensional equations of motion of the typical aerofoil section are given in Eqs. (1) and (2) which can be transformed into first order state-space ODEs by writing

$$\hat{\mathbf{x}}' = \mathbf{g}(\mathbf{x}, \hat{\mathbf{x}}), \tag{39}$$

where $\mathbf{x} = \{x_1, x_2, \ldots, x_{12}\}^{\mathrm{T}}$, and $\hat{\mathbf{x}} = \{\alpha, \alpha', \xi, \xi'\}^{\mathrm{T}} = \{x_{13}, x_{14}, x_{15}, x_{16}\}^{\mathrm{T}}$ are the states representing the motion of the aerofoil. Finally, the four additional ODEs for states 13–16 must be appended to the LB model state-space formulation as defined in Eqs. (3) and (4) to complete the aeroelastic system of 16 ODEs.

5. Analysis of the aeroelastic response

The main objectives of this section are to present numerical simulations of the aeroelastic behaviour of a NACA0012 aerofoil section, to analyse them using the tools of the theory of dynamical systems, to discuss the role of the nonsmooth definition of the aerodynamic loads into its complex dynamic behaviour and, finally, to address the important numerical issues associated with the nonsmoothness of the system.

Unless otherwise stated, the aerofoil has the following characteristics: $\mu = 100$, $x_\alpha = 0.25$, $a_h = -0.50$, $r_\alpha = 0.50$, $C_{M0} = -0.004$, $\bar{\omega} = 0.80$, and $\zeta_\alpha = \zeta_\xi = 0$. This is a symmetric aerofoil and the moment coefficient at zero incidence C_{M0} should be zero but here a small value of -0.004 has been adopted instead to break the symmetry of the system and make it more generic (Galvanetto, 2002).

All the bifurcation diagrams presented here show the steady-state local maxima of the angle α in the vertical axis. These have been obtained using a simple brute force technique where the time evolution of α is calculated for a set of values within the range of the control parameter, e.g. the free-stream Mach number M. Our results are numerically converged in the sense that reducing the time step or the various tolerances of the time integration routines does not lead to any significant changes in the values shown in the bifurcation diagrams. The accuracy of the time integration is further discussed in Section 5.1.

The Mach number has been varied in a relatively small range of values between 0.310 and 0.322 and the relevant bifurcation diagram is shown in Fig. 2(a). It shows that for small values of the Mach number, there exists a fixed point which loses its stability at $M \approx 0.3107$. This is a Hopf bifurcation where a periodic motion of amplitude increasing with Mach number is generated.

An enlarged view of the bifurcation diagram in the range of $0.316 \leqslant M \leqslant 0.318$ is shown in Fig. 2(b). The periodic motion generated at the Hopf bifurcation seems to disappear for $M \approx 0.3167$ which corresponds to point 2 in Fig. 2(b). At least two periodic attractors coexist in the range $0.31615 \leqslant M \leqslant 0.31670$. A second periodic motion is characterized by a maximum value of α close to 16.5°. Numerical computations show that, in the range $0.31694 \leqslant M \leqslant 0.31713$, this periodic motion coexists with a nonperiodic attractor. For larger values of the Mach number, only a nonperiodic motion has been found.

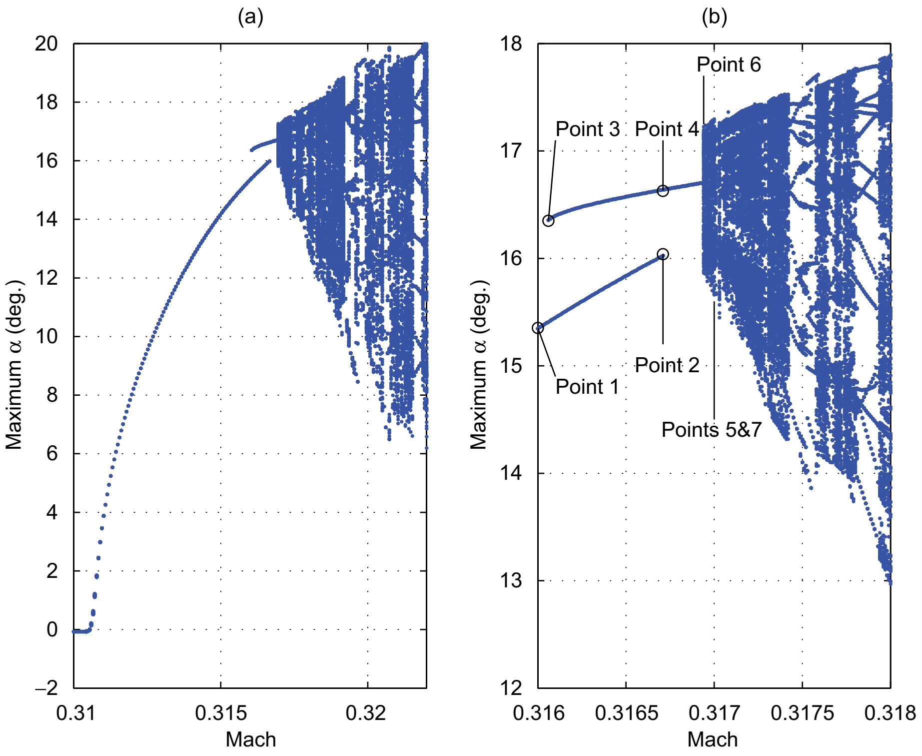

Fig. 2. Bifurcation diagrams: (a) $0.310 \leqslant M \leqslant 0.322$; (b) $0.316 \leqslant M \leqslant 0.318$. Points 3, 4 and 5 belong to the same branch of periodic attractors. Points 6 and 7 are nonperiodic attractors.

Section 3 shows that discontinuities affect the dynamic stall model when the state variable x_9 assumes the values $\pm C_{N1}$, and when x_{10} crosses the value $x_{10} = 0.70$. For this reason, the plane $x_9 - x_{10}$ is the most suitable to illustrate the interaction between the dynamics of the model and its discontinuities.

Fig. 3(a) shows the trajectory of one motion corresponding to point 2 in Fig. 2(b). This trajectory and those of all the motions corresponding to the points between points 1 and 2, are characterized by the fact that they do not intersect with the values $x_9 = \pm C_{N1}$ or $x_{10} = 0.70$. As the Mach number increases, the trajectory of the motion approaches the boundaries $x_9 = \pm C_{N1}$. It is assumed that the attractor disappears when its trajectory becomes tangent to the line $x_9 = -C_{N1}$.

Fig. 3(b) shows a trajectory of a motion belonging to the upper periodic branch of the bifurcation diagram of Fig. 2(b). The phase plot clearly shows that the trajectory does cross the vertical lines indicating $x_9 = \pm C_{N1}$, and numerical computations confirm that this is the case for all motions belonging to the branch of points 3-4-5 in Fig. 2(b). For increasing values of the Mach number, the amplitude of the motion grows and the trajectory approaches the other discontinuity line $x_{10} = 0.70$, but intersections between the attractor and the line $x_{10} = 0.70$ have not been detected.

Finally, Fig. 3(c) shows a trajectory for point 6 in Fig. 2(b). It is a nonperiodic motion the trajectory of which intersects all discontinuity lines $x_9 = \pm C_{N1}$, and $x_{10} = 0.70$, feature common to all motions of the nonperiodic branch.

Fig. 3(b) and (c) clearly show that the gradient of the trajectory is not continuous across the discontinuity lines represented by $x_9 = \pm C_{N1}$ and $x_{10} = 0.7$. This is because the parameters T_f, T_v, and α_1 have different values in different regions of the phase space.

The application of semi-empirical models beyond the conditions and range of parameters for which validation has been accomplished (harmonic oscillation) can obviously be questioned. However, a somewhat partial justification of the use of the LB-model in nonperiodic regimes can be derived from the time histories of the motion corresponding to points 2 and 6 of Fig. 2(b) depicted in Fig. 3. It is apparent that the nonperiodic motion of point 6 is not "very irregular". It is dominated by the same frequency as the motion of point 2 and the fluctuation of the amplitudes is small compared to the amplitudes themselves. Therefore, we assume that the parameter values employed to match the experimental periodic motions are correct for the nonperiodic trajectories.

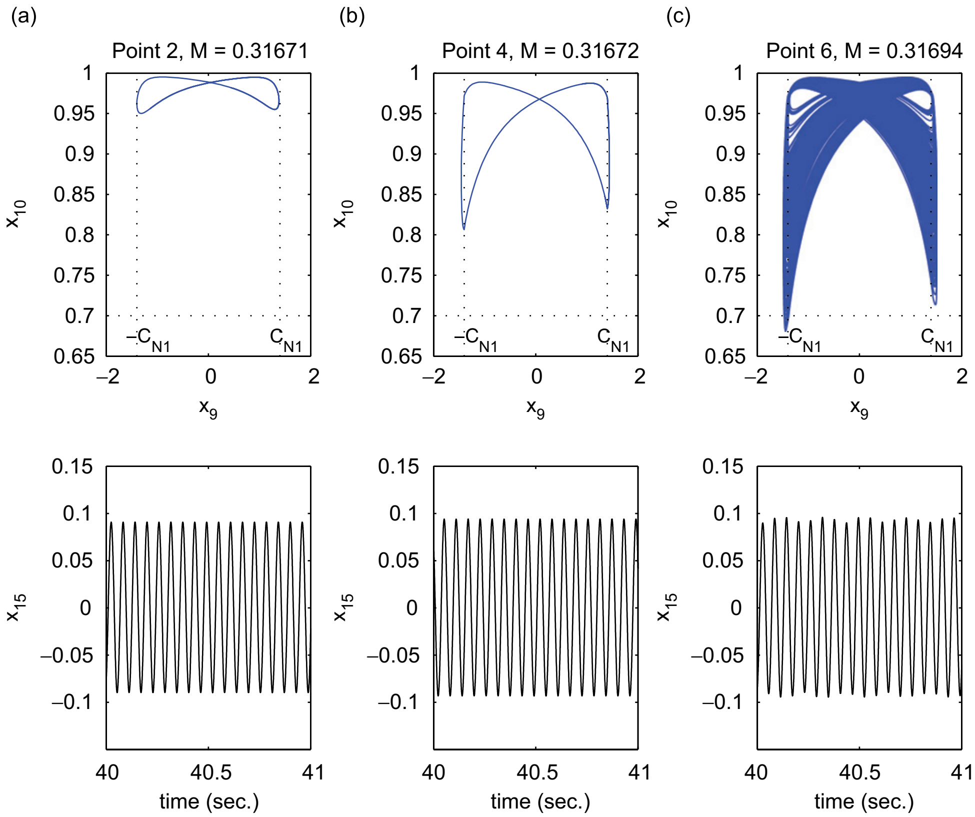

Fig. 3. Phase plots of x_9 and x_{10} (top) and time histories of angle of incidence (bottom) for: (a) point 2 in Fig. 2(b); (b) point 4 in Fig. 2(b); (c) point 6 in Fig. 2(b).

Another important issue raised by our results is that for the same set of parameter values motions of different nature may exist. In similar cases the steady state onto which a trajectory is attracted depends on its initial conditions. Coexisting attractors imply the existence of the relevant basins of attraction. The dynamical system under investigation is a 16-dimensional autonomous system therefore its basins of attraction have dimension 16 and cannot be easily visualized. However, it is possible to project the basins of attraction on any plane of two of the 16 state variables to have a graphical representation of the basins. The basins of attraction are projected in the plane of the physical variables α and ξ. A grid of initial conditions for α and ξ is chosen in the window: $0.1 \leqslant \alpha \leqslant 0.4$ and $0.05 \leqslant \xi \leqslant 0.15$. Each point of the grid will then be integrated in time to determine their resulting steady states. The points of the grid originating motions attracted by the nonperiodic attractor are marked with a circle in Fig. 4, whereas the initial conditions of motions ending up on the periodic attractor are left blank. The triangle in Fig. 4 is the trace of the periodic attractor, which appears to be close to the basin boundary.

5.1. Remarks on the importance of event detection

Our results have been obtained with the Matlab routine `ode45` equipped with optional event detection. The trajectory is continuously monitored so that when it intersects a discontinuity (for example $x_9 = \pm C_{N1}$) in the phase space, the intersection is accurately located and the correct system of differential equations is always integrated. The theory behind this technique and its implementation within Matlab are described by Moler (1997). Fig. 5 compares the solutions obtained with the *event detection* algorithm against those without event detection. The tolerance of the integration routine equipped with the event detection is $10^{-8}x_i$, where x_i is the current value of $x(t)$. The figure shows that the solution of the standard `ode45` approaches the one obtained with the event detection algorithm only after the tolerance is reduced by 4 orders of magnitude. The computational times, relative to those of the algorithm with event detection, required by the standard algorithm to integrate a time span of 20 s at $M = 0.31924$ for values of the tolerance

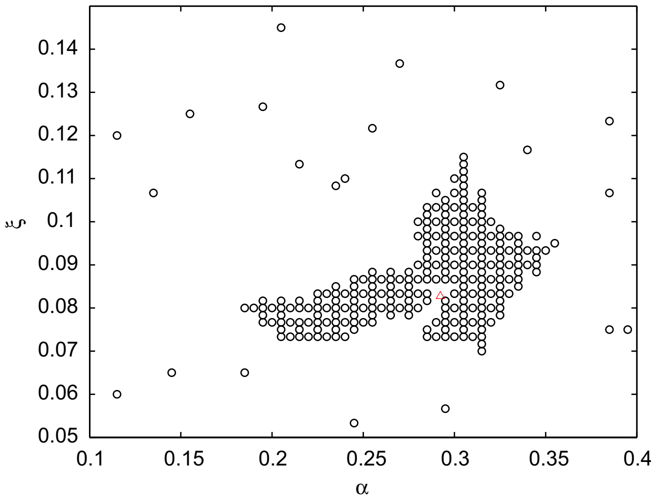

Fig. 4. Basins of attraction on the $x_{13} - x_{15}$ ($\alpha - \xi$) plane at $M = 0.3171$.

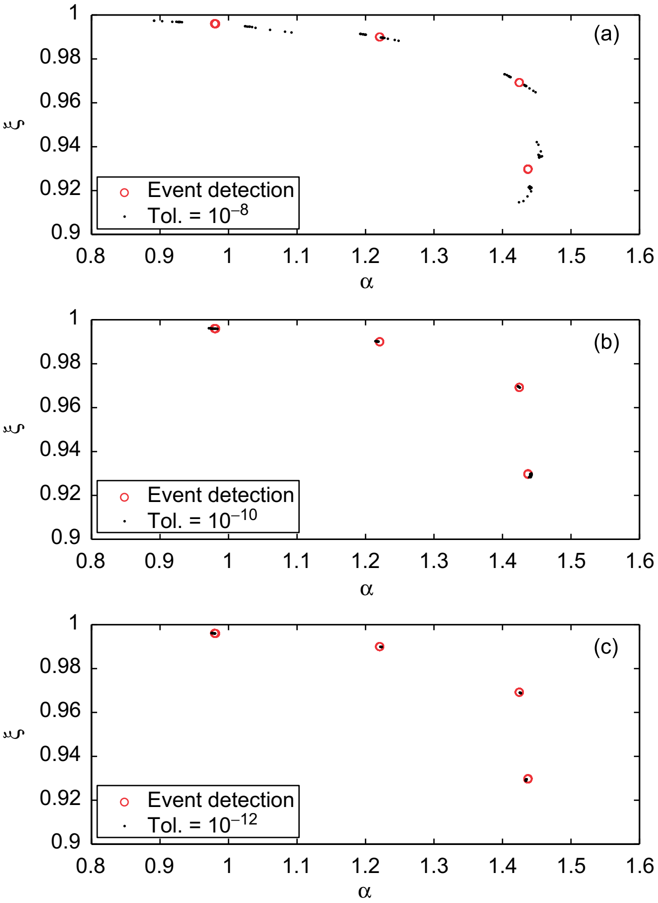

Fig. 5. Poincaré maps at $M = 0.31924$ for systems with event detection and without at different values of tolerances: (a) tol. $= 10^{-8}$, (b) tol. $= 10^{-10}$, and (c) tol. $= 10^{-12}$.

of 10^{-8}, 10^{-10} and 10^{-12}, are 1.3, 3.2 and 14.4, respectively. This clearly shows the benefit of incorporating event detection in the time integration of the aeroelastic system if high accuracy is a concern.

6. Conclusions

This paper presents an investigation of the dynamics of a typical aerofoil section in dynamic stall conditions. The popular LB dynamic stall model has been chosen to describe the aerodynamic forces. We have shown that the discontinuities in the definition of the model have a strong effect on the dynamics of the system.

A few empirical remarks can be made on the results presented in this paper, in particular on the motions shown in Fig. 2(b). This figure shows the evolution of three main attractors as the Mach number is varied. The first attractor, represented by points 1 and 2 in the figure, is a periodic motion generated at a Hopf bifurcation, its trajectories do not intersect any discontinuity and when that happens the attractor seems to disappear. The second attractor, represented by points 3, 4 and 5, is also periodic. It is not clear how it is generated and then destroyed, but its trajectories seem to be always characterized by intersections with the discontinuity at $x_9 = \pm C_{N1}$. Finally a nonperiodic attractor exists, corresponding to point 6 of Fig. 2(b), and its trajectories intersect both discontinuities at $x_9 = \pm C_{N1}$ and $x_{10} = 0.7$. Therefore, numerical evidence suggests that the discontinuous definition of the dynamic stall model has a considerable impact on the dynamics of the aeroelastic model. Different attractors seem to be characterized by different intersections with the discontinuities and some of the bifurcations seem due to the collision of steady-state trajectories with discontinuities.

Moreover, from an engineering point of view, the numerical simulations show that the computer model presents a remarkable sensitivity to small changes in the value of the Mach number. In a range which would probably be too small for a detailed experimental investigation, the model exhibits a large number of bifurcations and coexisting attractors. It is not clear to the authors if such a complexity could be a reflection of true physical facts or it is simply a consequence of mathematical artifacts.

Finally, the above-mentioned discontinuities require a careful numerical integration of the system. Numerical evidence is presented which shows how event detection algorithms are particularly useful to obtain high numerical accuracy without excessively increasing the integration time. To the best of our knowledge, comprehensive rotor analysis codes for rotorcraft and wind turbines based on the LB model, or other semi-empirical dynamic stall models, do not use event detection and therefore large numerical errors may be associated to the time steps in which the trajectory moves across the discontinuities in the definition of the model. A simpler way to reduce such an error would be to reduce the timestep in the algorithm for time integration, but this could lead to prohibitively expensive computing times.

Acknowledgements

The authors would like to thank Prof. Stefano Lenci of Università Politecnica delle Marche, Ancona, Italy, for useful discussions.

Appendix A. Attached flow components

The constant matrices in Eq. (18) are given by

$$\mathbf{A} = \mathrm{diag}[a_{11}\ \ a_{22}\ \ a_{33}\ \ a_{44}\ \ a_{55}\ \ a_{66}\ \ a_{77}\ \ a_{88}], \quad \mathbf{B} = \begin{bmatrix} 1 & 1 & 1 & 0 & 1 & 1 & 0 & 0 \\ \frac{1}{2} & \frac{1}{2} & 0 & 1 & 0 & 0 & 1 & 1 \end{bmatrix}^{\mathrm{T}}.$$

The elements in $\mathbf{A}$ are

$$a_{11} = -\frac{2V}{c} b_1 \beta^2, \quad a_{22} = -\frac{2V}{c} b_2 \beta^2, \quad a_{33} = -\frac{1}{K_\alpha T_I}, \quad a_{44} = -\frac{1}{K_q T_I},$$

$$a_{55} = -\frac{1}{b_3 K_{\alpha M} T_I}, \quad a_{66} = -\frac{1}{b_4 K_{\alpha M} T_I}, \quad a_{77} = -\frac{2V}{c} b_5 \beta^2, \quad a_{88} = -\frac{1}{K_{qM} T_I},$$

Table 1
NACA0012 aerofoil parameters as functions of the free-stream Mach number

Mach number	0.30	0.4	0.5	0.6	0.7	0.75	0.8
$C_{N\alpha}^S$	6.6211	7.0502	7.5100	8.2457	9.6864	10.9432	13.6407
α_{10}	0.2529	0.2073	0.1741	0.1409	0.0929	0.0580	0.0116
$\delta\alpha_1$	0.0367	0.0349	0.0253	0.0175	0.0140	0.0035	0.0017
S_1	0.0262	0.0284	0.0305	0.0349	0.0393	0.0305	0.0061
S_2	0.0201	0.0140	0.0105	0.0061	0.0044	0.0070	0.0016
K_0	0.0125	0.0300	0.1000	0.1900	0.1500	0.0050	−0.0500
K_1	−0.108	−0.108	−0.100	−0.096	−0.072	−0.104	0.016
K_2	0.04	0.05	0.04	0.04	0.15	−0.02	−0.01
D_f	8.0	7.75	6.2	6.0	5.9	5.5	4.0
T_{f0}	3.0	2.5	2.2	2.0	2.0	2.0	2.0
T_P	1.7	1.8	2.0	2.5	3.0	3.3	4.3
T_{v0}	6.0	6.0	6.0	6.0	6.0	6.0	4.0
T_{vl}	5.25	6.75	6.75	6.75	6.75	6.75	6.75
C_{N1}	1.45	1.20	1.05	0.92	0.68	0.50	0.18

where

$$T_I = \frac{c}{a},$$

$$K_\alpha = \frac{0.75}{(1-M)+\pi\beta^2M^2(A_1b_1+A_2b_2)}, \quad K_q = \frac{0.75}{(1-M)+2\pi\beta^2M^2(A_1b_1+A_2b_2)},$$

$$K_{\alpha M} = \frac{A_3b_4+A_4b_3}{b_3b_4(1-M)}, \quad K_{qM} = \frac{7}{15(1-M)+3\pi\beta M^2b_5},$$

with $A_1 = 0.30$, $A_2 = 0.70$, $A_3 = 1.50$, $A_4 = -0.50$, $b_1 = 0.24$, $b_2 = 0.53$, $b_3 = 0.25$, $b_4 = 0.10$, and $b_5 = 0.50$.

Appendix B. Parameters of the LB model

The parameters used for our interpretation of the LB model are given in Table 1. The parameters are those given by Leishman and Beddoes (1986) but some of them have been slightly modified to achieve a better fit to experimental data (McCroskey et al., 1976).

References

Beddoes, T.S., 1983. Representation of airfoil behaviour. Vertica 7 (2), 183–197.

Björck, A., 2000. DYNSTALL: subroutine package with a dynamic stall model. Technical Report FFAP-V-110, The Aeronautical Research Institute of Sweden.

Burton, T., Sharpe, D., Jenkins, N., Bossanyi, E., 2001. Wind Energy Handbook. Wiley, New York.

Chantharasenawong, C., 2007. Nonlinear aeroelastic behaviour of airfoil under dynamic stall. Ph.D. Thesis, Department of Aeronautics, Imperial College London.

Crouse, G.L., Leishman, J.G., 1992. Transonic aeroelasticity analysis using state-space unsteady aerodynamic modeling. Journal of Aircraft 29 (1), 153–160.

di Bernardo, M., Budd, C., Champneys, A., Kowalczyk, P., 2007. Bifurcation and Chaos in Piecewise-smooth Dynamical Systems: Theory and Applications. Applied Mathematical Sciences. Springer.

Ericsson, L.E., Reding, J.P., 1988. Fluid mechanics of dynamic stall. Part 1: unsteady flow concepts. Journal of Fluids and Structures 2, 1–33.

Fung, Y.C., 1993. An Introduction to the Theory of Aeroelasticity. Dover, New York.

Galvanetto, U., 2002. Some remarks on the two-block symmetric Burridge-Knopoff model. Physical Letters A 293, 251–259.

Gangwani, S.T., 1982. Prediction of dynamic stall and unsteady airloads for rotor blades. Journal of the American Helicopter Society 27, 57–64.

Gormont, R.E., 1973. A mathematical model of unsteady aerodynamics and radial flow for application to helicopter rotors. Technical Report TR 72-67, USAAV Labs.

Hansen, M.H., Gaunaa, M., Madsen, H.A., 2004. A Beddoes–Leishman type dynamic stall model in state-space and indicial formulation. Technical Report Risø-R-1354(EN), Risø National Laboratory, Roskilde, Denmark.

Johnson, W., 1970. The response and airloading of helicopter rotor blades due to dynamic stall. Massachusetts Institute of Technology ASRL TR 130-1.

Larsen, J.W., Nielsen, S.R.K., Krenk, S., 2007. Dynamic stall model for wind turbine airfoils. Journal of Fluids and Structures, 23 (7), 959–982.

Lee, B.H.K., Price, S.J., Wong, Y.S., 1998. Nonlinear aeroelastic analysis of airfoils: bifurcation and chaos. Progress in Aerospace Sciences 35, 205–334.

Leishman, J.G., 2006. Principles of Helicopter Aerodynamics, second ed. Cambridge University Press, Cambridge, MA.

Leishman, J.G., Beddoes, T.S., 1986. A generalised model for airfoil unsteady aerodynamic behaviour and dynamic stall using the indicial method. In: Proceedings of the 42nd Annual Forum. American Helicopter Society, Washington, DC.

Leishman, J.G., Beddoes, T.S., 1989. A semi-empirical model for dynamic stall. Journal of the American Helicopter Society 34, 3–17.

Leishman, J.G., Crouse, G.L., 1989. State-space model for unsteady airfoil behaviour and dynamic stall. In: Proceedings of the AIAA/AHS/ASME Structural Dynamics and Materials Conference, Mobile, Alabama, AIAA paper 89-1319.

Leishman, J.G., Nguyen, K.Q., 1988. State-space representation of unsteady airfoil behaviour. AIAA Journal 28 (5), 836–844.

Li, X.G., Fleeter, S., 2003. Dynamic stall generated airfoil oscillations. International Journal of Turbomachinery and Jet Engines 20, 217–233.

Mahajan, A.J., Kaza, K.R.V., Dowell, E.H., 1993. Semi-empirical model for prediction of unsteady forces on an airfoil with application to flutter. Journal of Fluids and Structures 7 (1), 87–103.

McCroskey, W.J., 1982. Unsteady airfoils. Annual Review of Fluid Mechanics 14, 285–311.

McCroskey, W.J., Carr, L.W., McAlister, K.W., 1976. Dynamic stall experiments on oscillating airfoils. AIAA Journal 14 (1), 57–63.

Moler, C., 1997. Are we there yet? Zero-crossing and event handling for differential equations. Matlab News and Notes Simulink 2 special ed., pp. 16–17.

Parameswaran, V., Baeder, J.D., 1995. Reduction of blade vortex interaction noise using prescribed pitching. In: Proceedings of the 13th AIAA Applied Aerodynamics Conference.

Petot, D., 1989. Modélisation du décrochage dynamique. La Recherche Aérospatiale 5, 60–72.

Price, S.J., Keleris, J.P., 1996. Non-linear dynamics of an airfoil forced to oscillate in dynamic stall. Journal of Sound and Vibration 194 (2), 265–283.

Shampine, L.F., Reichelt, M.W., 1997. The MATLAB ODE suite. SIAM Journal on Scientific Computing 18 (1), 1–22.

Shampine, L.F., Gladwell, I., Brankin, R.W., 1991. Reliable solution of special event location problems for ODEs. ACM Transactions on Mathematical Software (TOMS) 17, 11–25.

Tan, C.M., Carr, L.W., 1996. The AFDD international dynamic stall workshop on correlation of dynamic stall models with 3-D dynamic stall data. NASA Technical Memorandum 110375.